Multi-field Peeling-ballooning modes simulation

T. Y. Xia[1,2], X. Q. Xu[2], Z. X. Liu[1], S. C. Liu[1], B. Gui[1,2] and J. G. Li[1]

[1]Institute of Plasma Physics, Chinese Academy of Sciences, Hefei, China
[2]Lawrence Livermore National Laboratory, Livermore, CA 94550, USA

Corresponding Author: xiaty@ipp.ac.cn

Abstract:
The simulations on ELMs with Multi-field peeling-ballooning (P-B) mode using BOUT++ code are reported in this paper. In the purpose of studying the particle and energy transport in the pedestal region, the pressure equation is separated into ion density, ion and electron temperature equations. Through the simulations, the length scale L_n of the gradient of equilibrium density n_{i0} is found to destabilize the P-B modes in ideal MHD model. With diamagnetic effects, the growth rate is inversely proportional to n_{i0} at medium toroidal mode number n. For the nonlinear simulations, the gradient of n_{i0} in the pedestal region can increase the ELM size more than doubled. The six-field model based on full Braginskii equations are developed for the purpose of studying turbulence caused by drift waves. This model can localize the perturbations at peak gradient region compared with five-field model.

1 Introduction

To assess the performance requirements of future tokamaks, such as ITER, one must study [1] discharges in the high edge particle and energy confinement regime known as H-mode [2]. In ELMy H-mode, localized edge modes (ELMs) are triggered by ideal MHD instabilities. The type I ELM is successfully explained by ideal peeling-ballooning (P-B) theory in the pedestal [3], whereby the steep pressure gradients drive ballooning modes and bootstrap current generates peeling modes. The linear understanding of the P-B mode has been well developed by study with numerical codes such as ELITE [4, 5] and GATO [6]. However, linear stability analysis alone is not enough to describe the whole picture of ELM physics. The nonlinear phase is also very important for ELM studies. Some 3D codes have been developed for the nonlinear simulation of ELMs, including NIMROD [7, 8], BOUT [9, 10], JOREK [11], etc..

The BOUT++ code has successfully simulated the nonlinear crash phase of ELMs [12, 13, 14, 15]. In the previous work, anomalous electron viscosity or hyper-resistivity is applied into Ohm's law. This method resolves the computational difficulty of the fine resolution requirement for ideal MHD instabilities with high Lundquist number. The four-field two-fluid model has been developed as the extension of the previous three-field

peeling-ballooning model with the addition of perturbed parallel velocity [16]. The $E \times B$ shear flow plays a dual role on peeling-ballooning modes and they subsequently triggered ELM crashes [17].

In this paper we develop the nonlinear simulations of five-field peeling-ballooning model with BOUT++ code based on the reduced MHD model [18]. The inhomogeneous effects of ion density is taken into the considerations. The evolving variables are ion density, ion temperature, electron temperature, vorticity and magnetic flux. In order to simulate the physics in real tokamaks, including P-B modes and turbulence caused by electron drift waves and ion acoustic waves, the six-field two-fluid model based on Braginskii equations are also presented. Both linear and nonlinear simulation results will be discussed.

This paper is organized in the following way. In Sec. 2 the dynamic equations of five-field model and both linear and nonlinear simulations are introduced. Sec. 3 shows the simulation results of six-field model. Sec. 4 is the conclusion.

2 Five-field simulations

2.1 Theoretic equations

The five-field two-fluid nonlinear equations are applied to simulate the plasma edge pedestal collapse of tokamak in our model. Based on the peeling-ballooning model with non-ideal physics effects, including diamagnetic drift, $E \times B$ drift, resistivity and hyper-resistivity, a set of nonlinear evolution equations for perturbations of the ion number density n_i, ion temperature T_i, electron temperature T_e, vorticity ϖ and magnetic flux ψ is written as

$$\frac{\partial n_i}{\partial t} + \mathbf{V}_E \cdot \nabla n_i = 0, \tag{1}$$

$$\frac{\partial T_j}{\partial t} + \mathbf{V}_E \cdot \nabla T_j = \nabla_\parallel \left(\kappa_{\parallel j} \nabla_\parallel T_j \right), \tag{2}$$

$$\frac{\partial}{\partial t}\varpi + \mathbf{V}_E \cdot \nabla \varpi = B_0 \mathbf{b} \cdot \nabla \frac{J_\parallel}{B_0} + 2\mathbf{b}_0 \times \boldsymbol{\kappa} \cdot \nabla P, \tag{3}$$

$$\frac{\partial \psi}{\partial t} = -\frac{1}{B_0}\mathbf{b} \cdot \nabla \Phi + \frac{\eta}{\mu_0}\nabla_\perp^2 \psi - \frac{\eta_H}{\mu_0}\nabla_\perp^4 \psi, \tag{4}$$

$$\varpi = n_{i0}\frac{m_i}{B_0}\left[\nabla_\perp^2 \phi + \frac{1}{n_{i0}}\nabla_\perp \phi \cdot \nabla_\perp n_{i0} + \frac{1}{n_{i0} Z_i e}\nabla_\perp^2 p\right]. \tag{5}$$

Here the magnetic flux $\psi = A_\parallel / B_0$, $A_\parallel$ is the parallel vector potential, $\mathbf{b} = \mathbf{b}_0 + \nabla\psi \times \mathbf{b}_0$ and $\kappa = \mathbf{b}_0 \cdot \bigtriangledown \mathbf{b}_0$. $J_\parallel = J_{\parallel 0} - \frac{1}{\mu_0}\nabla_\perp^2 (B_0 \psi)$, $\mathbf{V}_E = \frac{1}{B_0}\left(\mathbf{b}_0 \times \nabla_\perp \Phi\right)$, $P = k_B n (T_i + T_e)$ and $\Phi = \Phi_0 + \phi$. The hyper-resistivity η_H, also called anomalous electron viscosity, could be significant for collisionless cases. The total time derivative is $\frac{d}{dt} = \frac{\partial}{\partial t} + \mathbf{v}_E \cdot \bigtriangledown$. Here for the simple model, both equilibrium flow and turbulent zonal flow have been set to be zero. The coefficients $\kappa_{\parallel j}$ in Eq. (2) are the parallel thermal conductivity for j particle, and will be discussed lately. The Eqs. (1) - (5) are solved within the field aligned (flux)

coordinate system (x, y, z) with the shift radial derivatives [13]. Notice that this model is the simplest form with nonlinear effects to specify the influences of density during the ELM crash clearly. The electron Hall effects, compressible terms and energy flux are all neglected for this reason.

The inner boundary conditions on x direction used here are Neumann for n_i, T_j and ϖ, and their outter boundary is Dirichlet. The boundary for ψ is zero-Laplacian and ϖ is Dirichlet on both inner and outter boundary. For all variables, the y direction is twisted-shifted periodic and z is periodic. The initial perturbation is Gaussian on x and y directions, and sinusoidal on z direction.

2.2 Simulation results

The shifted circular cross-section toroidal equilibria (cbm18_dens8) with the aspect ratio of 2.9 generated by TOQ code[19] is applied in this paper. In the analysis below, we choose the analytical profiles of n_{i0} as

$$n_{i0}(x) = \frac{(n_{0height} \times n_{ped})}{2}\left[1 - \tanh\left(\frac{x - x_{ped}}{\Delta x_{ped}}\right)\right] + n_{0ave} \times n_{ped}, \tag{6}$$

here n_{ped} is the ion number density on the top of the pedestal region, n_{0ave} is the ratio to control the bottom amplitude of n_{i0} outside the separatrix, and $n_{0height}$ is the coefficient to specify the gradient of n_{i0}. x_{ped} and Δx_{ped} represent the position of peak gradient and the width of pedestal region of P_0 respectively.

In this five-field model, the most important difference is the introduction of the the second term in RHS of Eq. (5), which represents the density length scale. This term still appears in ideal MHD model when the density profile varies spatially, especially in radial direction. Based on the localized analysis from Eqs. (1) to (5), the linear growth rate can be written as

$$\frac{\gamma_{Tc}}{\omega_A} = -\frac{iIm(\omega_{Tc})}{\omega_A} \simeq \frac{\gamma_{nc}}{\omega_A}\left(1 + \frac{1}{8k_\perp^2 L_n^2}\right), \tag{7}$$

where γ_{nc} is the growth rate for ideal MHD when density is spatially homogeneous. $L_n = \frac{1}{n_{i0}}\frac{\partial n_{i0}}{\partial r}$ is the characteristic length scale of ion density. Notice that $k_\perp^2 L_n^2 \sim 10^4 \gg 1$. Eq. (7) shows that if the gradient of n_{i0} is considered, the normalized linear growth rate is affected by $1/L_n^2$. In simulations, the different density profiles with different radial gradient but the same value at peak gradient point are applied. The results are shown as the solid lines in the right panel of Fig. 1. The dashed lines are the theoretical fitting according to Eq. (7), and they are consistent with the simulations. Therefore, L_n can increase the linear growth rate.

The normalized linear growth rate γ/ω_A is independent of n_{i0} for the ideal MHD theory. In the simulations, the constant n_{i0} profiles are applied in the right panel of Fig. 1. For these lines, $n_{0height}$ from Eq. (6) are zero and n_{0ave} are chosen as shown in the figure. The dashed lines are the linear growth rates of ideal MHD model for these profiles. They are all the same no matter what value n_{i0} is. However, if the diamagnetic effects are

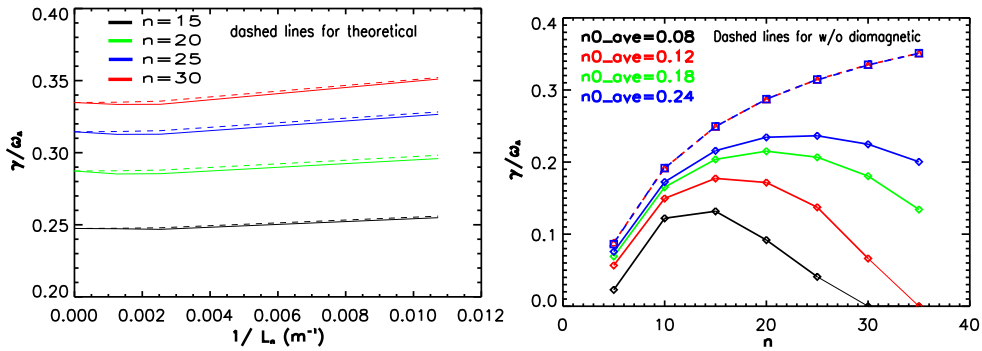

FIG. 1: Left: the normalized linear growth rate for different L_n in ideal MHD model. The dashed lines in right panel are the theoretical fitting according to Eq. (7). Right: the normalized linear growth rate for constant n_{i0} cases. The dashed lines are ideal MHD results.

taken into account, ω_* plays as the threshold of the perturbation [20]. Therefore, larger n_{i0} leads to smaller differences of γ/ω_A from ideal MHD results. This effect is also shown by the solid lines in the left panel of Fig. 1.

For the nonlinear simulations, we have to take the diamagnetic drift, resistivity and the anomalous electron viscosity into considerations [12]. The Lundquist number S and hyper Lundquist number S_H are set as $S = \mu_0 R_0 v_A/\eta = 10^8$ and $S_H = \mu_0 R_0^3 v_A/\eta_H = 10^{12}$, here S_H is introduced by hyper-resistivity. Five models with the different coefficients in Eq. (6) are chosen as: Case 0: $n_{0ave} = 0.12$, $n0_{height} = 0$; Case 1: $n_{0ave} = 0.02$, $n_{0height} = 0.24$; Case 2: $n_{0ave} = 0.02$, $n_{0height} = 0.30$; Case 3: $n_{0ave} = 0.02$, $n_{0height} = 0.45$ and Case 0': $T_{i0} = 1$keV. Notice that Case 0 is the same to the previous three-field model. Here we also consider the cases with the Dirichlet inner boundary condition on n_i, T_i and T_e for comparison, named as Case 1', 2' and 3', which have all the same coefficients and equilibrium profiles as Case 1, 2 and 3 respectively.

The left panel of Fig. 2 gives the radial pressure profiles in the outter mid-plane at $175T_A$ when all of the cases have passed through the nonlinear collapse phase. The perturbations for Case 0 are constraint at the pressure peak gradient region. However, for the other cases which include the gradient of n_{i0}, the collapse achieves the inner boundary, no matter what kind of boundary condition is applied. This indicates that the length scale term of Eq. (5), plays as an additional driving source of the electric potential ϕ on the perpendicular direction and drives the perturbations to go into the core region. The right panel of Fig. 2 shows the time evolution of ELM size in different models. Because of the penetrations, the ELM sizes are increased almost twice as the previous three-field model.

In order to study the energy flux on the divertor plate, the classical thermal conductivities $\kappa_{\|j}$ in collisional limit are necessary for this model. They are defined by

$$\kappa_{\|i} = 3.9\frac{v_{th,i}^2}{\nu_i}, \qquad \kappa_{\|e} = 3.2\frac{v_{th,e}^2}{\nu_e}, \tag{8}$$

where $v_{th,j}$ is the thermal velocity for j particle and ν_j is the collision rate. Since in hot pedestal the collisionality is low and $\kappa_{\|j}$ could be extremely larger than the real

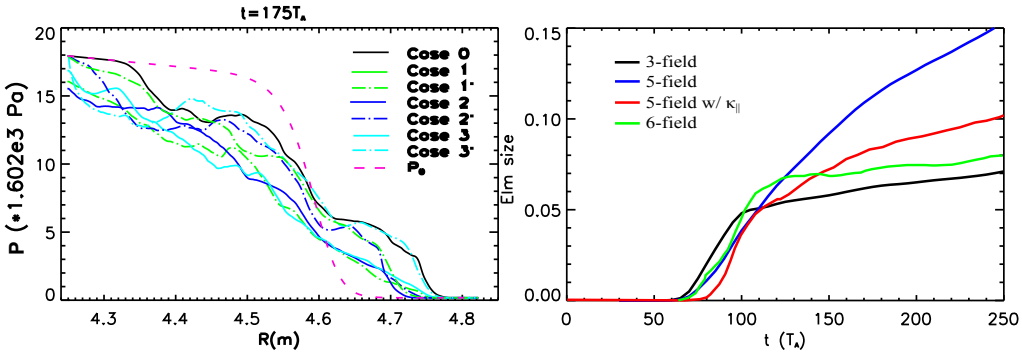

FIG. 2: Left: the pressure profiles after nonlinear crash at the outter mid-plane. Right: ELM size evolution for the previous three-field (black), five-field for Case 2(blue), five-field with $\kappa_{\|j}$ for Case 2 (red) and six-filed for Case 2 (green).

experiment, the flux limited expression $\kappa_{fl,j} = v_{th,j} q_{95} R_0$ is taken into account of kinetic effects. For the linear effects of thermal conductivities, γ/ω_A is decreased by around 25.0%. They can effectively decrease the growth of ELM size by 33.3%, as the red line shown in the right panel of Fig. 2. This is because that they can prevent the pressure perturbations to propagate to the inner boundary.

3 Six-field simulations

The six-field model is derived directly from Braginskii equations in drift ordering [21, 22]. The non-ideal MHD terms are all kept, such as energy flux, electron-ion friction forces, energy exchange and gyro-viscosity. The equations of this model are written as

$$\begin{aligned}\frac{\partial}{\partial t}\varpi &= -\left(\frac{1}{B_0}\boldsymbol{b}\times\boldsymbol{\nabla}_\perp\Phi\right)\cdot\boldsymbol{\nabla}\varpi + B^2\nabla_\|\left(\frac{J_\|}{B}\right) + 2\boldsymbol{b}\times\boldsymbol{\kappa}\cdot\boldsymbol{\nabla}P_i \\ &\quad -\frac{1}{2\Omega_i}\left[\frac{1}{B}\boldsymbol{b}\times\boldsymbol{\nabla}P_i\cdot\boldsymbol{\nabla}\left(\nabla_\perp^2\Phi\right) - Z_i e B\boldsymbol{b}\times\boldsymbol{\nabla}n_i\cdot\boldsymbol{\nabla}\left(\frac{\nabla_\perp\Phi}{B}\right)^2\right] \\ &\quad +\frac{1}{2\Omega_i}\left[\frac{1}{B}\boldsymbol{b}\times\boldsymbol{\nabla}\Phi\cdot\boldsymbol{\nabla}\left(\nabla_\perp^2 P_i\right) - \nabla_\perp^2\left(\frac{1}{B}\boldsymbol{b}\times\boldsymbol{\nabla}\Phi\cdot\boldsymbol{\nabla}P_i\right)\right], \end{aligned} \tag{9}$$

$$\begin{aligned}\frac{\partial}{\partial t}n_i &= -\left(\frac{1}{B_0}\boldsymbol{b}\times\boldsymbol{\nabla}_\perp\Phi\right)\cdot\nabla n_i \\ &\quad -\frac{2n_i}{B}\boldsymbol{b}\times\boldsymbol{\kappa}\cdot\boldsymbol{\nabla}\Phi - \frac{2}{Z_i e B}\boldsymbol{b}\times\boldsymbol{\kappa}\cdot\boldsymbol{\nabla}P - n_i B\nabla_\|\left(\frac{V_{\|i}}{B}\right), \end{aligned} \tag{10}$$

$$\frac{\partial}{\partial t}V_{\|i} = -\left(\frac{1}{B}\boldsymbol{b}\times\boldsymbol{\nabla}_\perp\Phi\right)\cdot\boldsymbol{\nabla}V_{\|i} - \frac{1}{m_i n_i}\nabla_\| P, \tag{11}$$

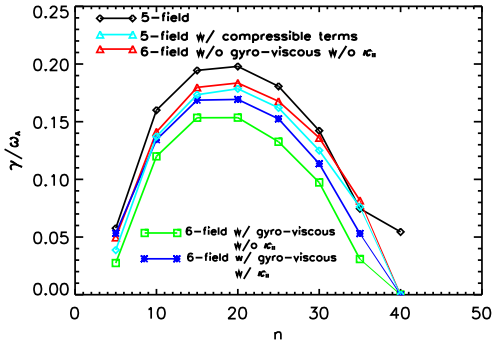

FIG. 3: The linear growth rate for five- and six-field models.

$$\frac{\partial}{\partial t}\psi = -\frac{1}{B}\nabla_{\parallel}\phi + \frac{\eta}{\mu_0}\nabla_{\perp}^2\psi + \frac{1}{en_eB}\nabla_{\parallel}P_e + \frac{0.71k_B}{eB}\nabla_{\parallel}T_e - \frac{\eta_H}{\mu_0}\nabla_{\perp}^4\psi, \tag{12}$$

$$\begin{aligned}\frac{\partial}{\partial t}T_i = & -\left(\frac{1}{B}\boldsymbol{b}\times\boldsymbol{\nabla}_{\perp}\Phi\right)\cdot\boldsymbol{\nabla}T_i + \frac{2m_e}{m_i}\frac{Z_i}{\tau_e}\left(T_e - T_i\right) \\ & -\frac{2}{3}T_i\left[\left(\frac{2}{B}\boldsymbol{b}\times\boldsymbol{\kappa}\right)\cdot\left(\boldsymbol{\nabla}\Phi + \frac{1}{Z_ien_i}\boldsymbol{\nabla}P_i + \frac{5}{2}\frac{k_B}{Z_ie}\boldsymbol{\nabla}T_i\right) + B\nabla_{\parallel}\left(\frac{V_{\parallel i}}{B}\right)\right] \\ & +\frac{2}{3n_ik_B}\nabla_{\parallel}\left(\kappa_{\parallel i}\nabla_{\parallel}T_i\right) + \frac{2}{3n_ik_B}\nabla_{\perp}\left(\kappa_{\perp i}\nabla_{\perp}T_i\right),\end{aligned} \tag{13}$$

$$\begin{aligned}\frac{\partial}{\partial t}T_e = & -\left(\frac{1}{B}\boldsymbol{b}\times\boldsymbol{\nabla}_{\perp}\Phi\right)\cdot\boldsymbol{\nabla}T_e \\ & -\frac{2}{3}T_e\left[\left(\frac{2}{B}\boldsymbol{b}\times\boldsymbol{\kappa}\right)\cdot\left(\boldsymbol{\nabla}\Phi - \frac{1}{en_e}\boldsymbol{\nabla}P_e - \frac{5}{2}\frac{k_B}{e}\boldsymbol{\nabla}T_e\right) + B\nabla_{\parallel}\left(\frac{V_{\parallel e}}{B}\right)\right] \\ & +0.71\frac{2T_e}{3en_e}B\nabla_{\parallel}\left(\frac{J_{\parallel}}{B}\right) - \frac{2m_e}{m_i}\frac{1}{\tau_e}\left(T_e - T_i\right) + \frac{2}{3n_ek_B}\eta_{\parallel}J_{\parallel}^2 \\ & +\frac{2}{3n_ek_B}\nabla_{\parallel}\left(\kappa_{\parallel e}\nabla_{\parallel}T_e\right) + \frac{2}{3n_ek_B}\nabla_{\parallel}\left(\kappa_{\perp e}\nabla_{\perp}T_e\right).\end{aligned} \tag{14}$$

Notice that the thermal conductivities is defined by Eq. (8) within flux limited expressions, and Spitzer resistivity are applied instead of constant Lundquist number in this model. Compared with five-field model, the most important differences is the appearance of parallel ion velocity equation. Another difference is the gyro viscosity, as shown in the last two lines of Eq. (9), which is added as the modification of gyro kinetic effects. Within this model, the studies of boundary turbulence caused by electron drift waves and ion acoustic waves are feasible, which are neglected in five- and three-field models.

For the linear simulations, Fig. 3 gives the comparison to five-field model. The profiles of density and temperature are chosen as Case 2 mentioned in Sec. 2.2. If taking out the gyro-viscous terms and $\kappa_{\parallel j}$, the six-field model can decrease γ/ω_A by 10.1%, most of the stabilizing effects are provided by the compressible terms, as $\boldsymbol{b}\times\boldsymbol{\kappa}\cdot\boldsymbol{\nabla}$ in Eqs. (10), (13) and (14), shown as the cyan line in Fig. 3. The gyro-viscous terms have obvious

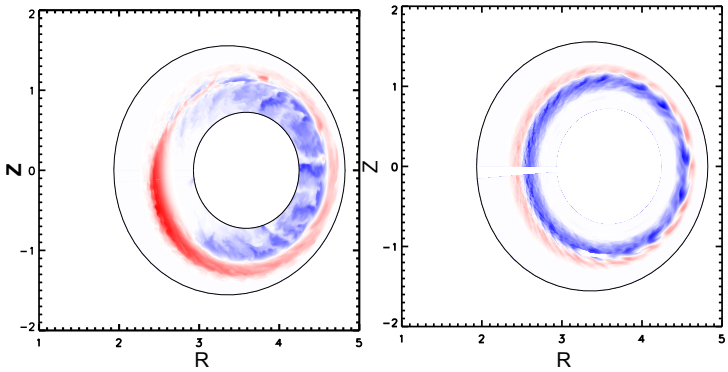

FIG. 4: Left: the density perturbation structures at saturating phase after ELM crash for five-field model, $t = 300T_A$. Right: the density perturbation structures at the same time for six-field model. Red means positive perturbation and blue is for negative.

stabilizing effects and decrease γ/ω_A by 16.7%. $\kappa_{\|j}$ dominates the electron temperature equations and increases it by 9.7%.

The ELM size is shown as the green line in the right panel of Fig. 2. Compared with five-field model, the ELM size is decreased by around 50.0% and is more similar to the three field simulations. The mode structures of ion density perturbations at saturating phase after ELM crash for both five-field and six-field are shown in Fig. (4). The left panel of six-field model shows much more narrow modes than five-field and no perturbations can arrive the inner boundary. Both the gyro-viscosity and thermal conductivities constrain the growth of perturbations at inner boundary.

4 Conclusions

The multi-field two-fluid model are developed for the peeling-ballooning simulations with BOUT++ code. This model introduces the effects of ion density profile, including both gradient and quantity of n_{i0}. The gradient length scale L_n of n_{i0} can slightly destabilize the perturbations for ideal MHD, but the larger n_{i0} leads to smaller differences of γ/ω_A from ideal model at medium mode number n, when diamagnetic effects are taken into account. For nonlinear simulations, L_n causes as twice ELM size as the previous model because it drives the perturbations to propagate into the inner boundary. This driving effects can be suppressed by either thermal conductivities effectively or full Braginskii six-field model. Compared with five-field model, the six-field model derives much smaller ELM size and more localized mode structures.

Acknowledgements

This work was performed under the auspices of the U.S. DoE by LLNL under Contract DE-AC52-07NA27344 and is supported by the China NSF under Contract No.10721505,

the National Magnetic Confinement Fusion Science Program of China under Contractsno.2011GB107001. LLNL-PROC-583395.

References

[1] E.J. Doyle et al., 22nd IAEA Fusion Energy Conf. (Geneva, Switzerland), (2008).

[2] M. Keilhacker et al., Plasma Phys. Control. Fusion **26**, 49 (1984).

[3] P.B. Snyder et al., Nucl. Fusion **49**, (2009).

[4] P.B. Snyder et al., Phys. Plasmas **9**,, 2037 (2002).

[5] H.R. Wilson et al., Phys. Plasmas **9**, 1277 (2002).

[6] L.C. Bernard, F.J. Helton and R.W. Moore, Comput. Phys. Commun. **24**, 377 (1981).

[7] C.R. Sovinec et al., J. Comput. Phys. **195**, 355 (2004).

[8] D.P. Brennan et al., J. Phys.: Conf. Ser. **46**, 63 (2006).

[9] P.B. Snyder, H.R. Wilson and X.Q. Xu, Phys. Plasmas **12**, 056115 (2005).

[10] P.B. Snyder, H.R. Wilson and X.Q. Xu, Nonlinear 3D simulations of ELMs with the BOUT code Fluid Modelling of ELMs Workshop (Boulder, CO, USA), (2006).

[11] G.T.A. Huysmans and O. Czarny, Nucl. Fusion **47**, 659 (2007).

[12] X. Q. Xu, B. Dudson *et al.,* Phys. Rev. Lett., **105**, 175005(2010).

[13] B. D. Dudson, H. R. Wilson, *et al.,* Comput. Phys. Commun. **180**, 1467(2009).

[14] X.Q. Xu, B.D. Dudson, P.B. Snyder, M.V. Umansky, H. Wilson and T. Casper, Nucl. Fusion. **51**, 103040 (2011).

[15] B. D. Dudson, *et al.*, Plasma Phys. Control. Fusion **53**, 054005 (2011).

[16] T.Y. Xia, X.Q. Xu, B.D. Dudson and J. Li, Contrib. Plasma Phys. **52**, No. 5-6, 353 (2012).

[17] P. W. Xi, X. Q. Xu, X. G. Wang, and T. Y. Xia, Phys. Plasmas **19**, 092503 (2012).

[18] R.D. Hazeltine and J.D. Meiss, Phys. Rep. **121**, 1 (1985).

[19] R. L. Miller and J. W. V. Dam, Nucl. Fusion **27**, 2101(1987).

[20] R. J. Hastie, J. J. Ramos, & F. Porcelli, Phys. Plasmas **10**, 4405 (2003).

[21] X. Q. Xu et al., Commun. Comput. Phys. **4**, 949 (2008).

[22] A. N. Simakov & P. J. Catto, Phys. Plasmas **10**, 4744 (2003).